Published in final edited form as:
Coord Chem Rev. 2013 January 15; 257(2): 528–540. doi:10.1016/j.ccr.2012.06.003.

Recent advances in phenoxyl radical complexes of salen-type ligands as mixed-valent galactose oxidase models

Christopher T. Lyons and **T. Daniel P. Stack**
Department of Chemistry, Stanford University, Sanford, CA 94305, United States

Christopher T. Lyons: ctlyons@stanford.edu

Abstract

The interplay between redox-active transition metal ions and redox-active ligands in metalloenzyme sites is an area of considerable research interest. Galactose oxidase (GO) is the archetypical example, catalyzing the aerobic oxidation of primary alcohols to aldehydes via two one-electron cofactors: a copper atom and a cysteine-modified tyrosine residue. The electronic structure of the oxidized form of the enzyme (GO_{ox}) has been investigated extensively through small molecule analogues including metal-salen phenoxyl radical complexes. Similar to GO_{ox}, one-electron oxidized metal-salen complexes are mixed-valent species, in which molecular orbitals (MOs) with predominantly phenolate and phenoxyl π-character act as redox-active centers bridged by mixing with metal *d*-orbitals. A detailed evaluation of the electronic distribution in these odd electron species using a variety of spectroscopic, electrochemical, and theoretical techniques has led to keen insights into the electronic structure of GO_{ox}.

Keywords

Phenoxyl radical; Galactose oxidase; Transition metals; Salen; Redox-active ligands; Electrochemistry; Spectroscopy; Electronic structure

1. Introduction

Over the last fifteen years, the study of metal-coordinated phenoxyl radicals has received much attention in the literature, in large part due to their biological relevance. The presence of a tyrosyl residue is well established in various metalloenzymes, including class I ribonucleotide reductase [1,2], prostaglandin endoperoxide synthase [3,4], photosystem II [5,6], cytochrome *c* oxidase [7,8], glyoxal oxidase [9], and galactose oxidase (GO) [10,11]. The latter three are particularly interesting examples of metal-ligand cooperativity in facilitating redox processes.

GO is a mononuclear copper enzyme that catalyzes the aerobic oxidation of primary alcohols to aldehydes, with subsequent reduction of dioxygen to H_2O_2 (Scheme 1) [11,12]. The coordination sphere contains two equatorial histidine residues (His496, His581), an axial unmodified tyrosine (Tyr495), and an equatorial tyrosine covalently cross-linked to a neighboring cysteine residue in an oxidative post-translational modification (Tyr272,

---

Corresponding Author: T. Daniel P. Stack stack@stanford.edu Phone: 650-725-8736 Fax: 650-725-0259.

Cys228) [13,14]. The catalytically relevant form of the enzyme (GO_{ox}) exists as a Cu^{II} modified tyrosyl radical species. Though copper typically participates in redox processes through a single electron Cu^{I}/Cu^{II} redox couple, the Cys cross-linked tyrosyl radical provides the second oxidizing equivalent necessary for catalytic alcohol oxidation. This redox cooperativity has inspired chemists for nearly two decades to design small molecule analogues of GO, contributing to the understanding of the enzymatic system and the development of ligand frameworks capable of storing oxidizing equivalents for use in multi-electron transformations.

Since the preparation of a stable Fe(III)-phenoxyl radical complex first reported by Wieghardt *et al.* in 1993, the number of small molecule metal-phenoxyl systems has grown to include a variety of metals in different ligand frameworks [15]. The focus in modeling GO has centered largely around the challenges associated with reproducing the reactivity and spectroscopic properties of the enzyme, and several excellent reviews highlighting this research are available [16-18]. More recently, interest in the mixed-valent state of GO_{ox} has developed, and in particular how the asymmetry in phenolate coordination inherent in the enzyme due to the cysteine crosslink of Tyr272 coupled to the axial/equatorial copper coordination effects the electronic structure of this tyrosyl radical species [19,20]. Delocalization of the “hole” onto the Cys cross link is suggested to stabilize GO_{ox} significantly ($t_{1/2}$ = 7.2 days) [11].

It is well established that oxidized metal-salen complexes can exist, in the limiting case, as either a high-valent metal species ($M^{n+1}L^{-}$) or a ligand radical ($M^{n}L^{\bullet}$) depending on the nature of the ligand-field and identity of the metal center. Interestingly, metal-salen phenoxyl radical complexes are mixed-valent species akin to GO_{ox}, in which MOs with predominantly phenolate and phenoxyl π-character act as redox centers bridged by mixing with metal *d*-orbitals. The radical could potentially localize on one-ring (Class I), partially delocalize (Class II), or fully delocalize (Class III), following the Robin-Day classification scheme [21-24]. The extent of radical delocalization is dependent heavily on the identity of the metal center and the structure of the phenolate, which can be derivatized with various substituents to influence the locus of oxidation by introducing electronic asymmetry into the ligand. Our presentation here focuses on metal-phenoxyl complexes of salen-type ligands, with particular attention paid to the characterization of metal-salen phenoxyl radical complexes as mixed-valent species.

2. Ligand Synthesis

Salen ligands are used extensively in coordination chemistry and catalysis, due to their relative ease of synthesis and propensity to ligate a variety of transition metal ions in a potentially chiral, tetradentate N_2O_2 coordination mode [25-27]. Ligands are typically synthesized by condensation of two equivalents of salicylaldehyde with one equivalent of diamine (Scheme 2). This condensation reaction allows for a wealth of symmetric salen-type ligands to be produced through the incorporation of various functional groups on the phenolate moieties and by introduction of various diamine linkers. Reduction of the imine bonds to afford symmetric N_2O_2 amino-phenolate containing salens (“reduced” salens) has also been developed (**4**, **5**, $\mathbf{13}^{R1,R2}$, Scheme 3) [20,28-30]. Addition of metal salts to solutions of salen ligands readily leads to complexation and formation of metal-salen complexes (M**X**, where M = metal and **X** = ligand, Scheme 3). Salen-metal complexes of Cu^{II}, Ni^{II}, and Zn^{II} are generally four coordinate, distorted planar structures. Increasing the carbon chain length of the diamine allows some Cu^{II} complexes to adopt nearly tetrahedral coordination geometries [31,32].

A synthetic procedure reported by Campbell and Nguyen opened up a vast area in salen ligand variation by allowing for the synthesis of ligands bearing dissimilar phenolates, greatly increasing the electronic and geometric diversity of available complexes (Scheme 4) [33]. This procedure, along with reduction of imino-phenolates and the ability of these ligands to coordinate a variety of transition metal ions, allows for nearly endless permutations of metal complexes. This development has proven particularly useful for GO modeling in that alkyl-sulfanyl substituents can be introduced non-symmetrically into the salen or reduced salen frameworks, providing greater structural and electronic fidelity to the enzyme [20]. In addition to ligands bearing dissimilar phenolate substitution, ligands containing both an amino- and an imino-phenolate moiety, subsequently referred to as "half-reduced" salen, can be accessed by adaptation of the synthetic procedure (Scheme 5). In this case, the presence of a single amino-phenolate provides electronic asymmetry to the ligand framework with identically substituted phenolate moieties. Throughout this review, complexes containing identical phenolates will be referred to as "symmetric", while complexes containing dissimilar phenolates will be referred to as "non-symmetric". The terms "symmetric" and "non-symmetric" are used simply for convenience and are not meant to imply any rigorous molecular point group assignment.

One crucial aspect of ligand design in this research area is the need for phenolate substitution in both the *ortho* and *para* positions to ensure stability of the phenoxyl radical complex generated upon oxidation. [34] Without such substitution, radical coupling of the phenoxyl radical species proceeds rapidly, even at temperatures as low as −125°C.

3. General Considerations

One-electron oxidation of metal-phenolate complexes can result, in the limiting case, in the formation of either a ligand radical ($M^nL^{\bullet}$) or a high-valent metal species ($M^{n+1}L^{-}$). Not surprisingly, localization of the hole on either the metal center or the ligand framework can lead to dramatic differences in spectroscopic and electrochemical properties. Determination of the locus of oxidation plays a central role in the characterization of these compounds and is crucial to the understanding of the interplay between ligand and metal electronic properties. Simply put, *where* and to *what extent* is the hole localized is the question asked. Various spectroscopic techniques and theoretical methods aid in addressing this question.

For a symmetric two-redox center system in the Class II regime, the two states that correspond to localization of the radical on one redox active moiety or the other are modeled by harmonic functions in a Marcus-Hush analysis of these odd electron species. These harmonic functions represent molecular vibrations that map onto the electron transfer coordinate. These diabatic states couple to form two adiabatic energy surfaces: a ground state surface whose two minima represent a partial localization of charge on each redox center, and an excited state surface with a single minimum (Figure 1a). The intervalence charge transfer (IVCT) band corresponds to the optically induced transition between the two adiabatic states, conceptualized as a phenolate-to-phenoxyl ligand-to-ligand charge transfer transition (Figure 2) [35]. These absorptions typically appear in the near infrared region (NIR, 800 - 2500 nm), and the band-shape parameters ν_{max}, ε_{max}, and $\Delta\nu_{1/2}$ are related to the reorganizational energy of the system, λ, and the electronic coupling constant, H_{AB}. For IVCT transitions, the absorption bandwidth is expected to increase with ν_{max} and $\Delta\nu_{HTL}$ according to equation 1. Importantly H_{AB} can be determined experimentally from the ν_{max}, ε_{max}, and $\Delta\nu_{1/2}$ of the IVCT band and an estimate of the electron transfer distance r_{CT} using the Hush equation (equation 2) [22].

$$\Delta\nu_{\mathrm{HTL}}=\sqrt{16\ln 2RT\nu_{\max}}=\sqrt{2310\nu_{\max}} \quad (1)$$

$$H_{AB}=2.06\times10^{-2}\,\frac{\sqrt{\epsilon_{\max}\Delta\nu_{1/2}\nu_{\max}}}{r_{CT}} \quad (2)$$

$$\begin{vmatrix} \lambda x^2-E & H_{AB} \\ H_{AB} & \lambda(1-x)^2+\Delta G^\circ-E \end{vmatrix}=0 \quad (3)$$

To extend the Marcus-Hush model to complexes with non-symmetric phenolates, the secular equation that defines the energy of the ground and excited state surfaces is perturbed by the addition of ΔG°, a term that represents the thermodynamic free energy difference between the two localized states (equation 3). For the non-symmetric model, the two minima of the ground state surface now lie at different energies, with the unpaired electron preferentially localized on the ring that was more readily oxidized (Figure 1b). The energy of the IVCT absorption is the sum of λ and ΔG°. Equations 1 and 2 for determining $\Delta\nu_{\mathrm{HTL}}$ and H_{AB} are applicable for both the non-symmetric and symmetric models. Compounds bearing dissimilar phenolates will necessarily tend toward a Class II, if not Class I, description because the thermodynamic differentiation of the phenolates will attenuate delocalization; symmetric complexes have a greater possibility of existing as Class III. In the Class III regime, the energy of the IVCT band conveniently provides a direct measure of H_{AB}, as $h\nu = 2H_{AB}$ [22].

4. Generation of phenoxyl radicals

A variety of chemical and electrochemical techniques are used to generate metal-salen phenoxyl radicals, allowing for the study of these intermediates. In most cases discussed herein, one-electron oxidation leads formally to a single phenoxyl radical rather than a high-valent metal species.

Metal-salen complexes are oxidized using a variety of common chemical oxidants (Table 1) [36]. Choice of oxidant will depend on specific reaction conditions and the potentials of the complexes. The use of oxidants with characteristic optical features is particularly helpful for spectrophotometric titration experiments and *in situ* optical monitoring of phenoxyl radical formation [19]. In general, metal-salen complexes containing amino-phenolates *(i.e.* M**4**, M**5**, M**13**^{R1,R2}) are more readily oxidized than their related imino-phenolate complexes because the former are more electron rich [20,29]. However, these amino-phenoxyl radical complexes are less stable than related imino-phenoxyl radicals at room temperature [29]. Potentiometric oxidation is another common method employed to generate the radical species [28,30,37,38]. The ionic strength of the medium in these experiments facilitates oxidation of salen complexes by comparison to spectrophotometric titrations, which are often performed in the absence of electrolyte. For example, the strong chemical oxidant [thianthrene]$^+$ (Th$^+$, Table 1) has a redox potential of + 880 mV vs. Fc/Fc$^+$ in CH_2Cl_2, but the two-electron oxidized [Cu**3**]$^{2+}$, with a second oxidation potential at 650 mV, is not accessible in the absence of electrolyte [19]. The presence of electrolyte or in some cases the counter-anion introduced via chemical oxidants may affect the spectroscopic properties of the phenoxyl species, as anions can associate with complexes, influencing the hole locus [39,40]. A recent report suggests that the identity of the electrolyte during electrochemical oxidations of iron complexes of salen-like ligands alters significantly the sequence of phenolate oxidation through ion pairing effects [41].

In most reports, CH_2Cl_2 is the preferred solvent for the preparation and study of metal-salen phenoxyl radical complexes. The weak ligating abilities of CH_2Cl_2 to metals helps to ensure that the salen ligands remain coordinated in solution upon oxidation to phenoxyl radicals, which are weaker donors than their parent anionic phenolates. This strategy may become less reliable when operating in high concentrations of electrolyte.

5. Characterization of oxidized salen complexes

5.1. X-ray crystallography

X-ray crystallography is a powerful technique for characterizing oxidized metal-salen complexes and assessing oxidation locus. The first phenoxyl radical complex structurally characterized by Wieghardt *et al.* (Figure 3), contains a chromium center, coordinated by two phenolates and one phenoxyl radical that differ significantly in their metrical parameters [42]. The Cr – O distance of the phenoxyl radical is elongated by 0.02 Å relative to the phenolates, while the metal bonded O – C bond of the phenoxyl radical is 0.12 Å shorter than the Cr-bonded phenolates; these metrical parameters are consistent with decreased donating ability and a quinoid-like structure for the phenoxyl ring, respectively (Figure 4). Though this metrical trend is useful for identifying phenoxyl radicals in certain systems, exceptions apply, particularly for phenoxyl radicals of salen complexes. For example, oxidation of Ni**3** with the hexafluoroantimonate (SbF_6^-) salt of either Ag^+ or Th^+ leads to the formation of $[Ni\mathbf{3}]^+SbF_6^-$, solutions of which are stable for weeks at room temperature under dinitrogen [40]. The solid-state structure of $[Ni\mathbf{3}]^+$ displays a symmetric coordination sphere *contraction*, a counterintuitive result given the decreased donating abilities of phenoxyl radicals relative to phenolates. A contraction seems more consistent with a metal-based oxidation. Further spectroscopic analysis combined with density functional theory (DFT) calculations support that $[Ni\mathbf{3}]^+$ exists as a phenoxyl radical complex and suggests that an electron is removed from a predominately ligand-based antibonding orbital, leading to the observed coordination sphere contraction [40].

Shimazaki and coworkers have extended work on Ni**3** to a series that includes the palladium and platinum complexes [43]. Unlike the symmetric contraction in the solid-state structures of the oxidized nickel and platinum complexes, $[Pd\mathbf{3}]^+$ displays a non-symmetric coordination, consistent with increased localization of the radical to one side of the molecule [43]. In a later report, the same trend was observed for the propyl-backbone series $[Ni\mathbf{8}]^+$, $[Pd\mathbf{8}]^+$, and $[Pt\mathbf{8}]^+$, even though the geometries are more distorted from a planar coordination due to the increased length of the diamine backbone [44]. This trend suggests that the identity of the metal center within a series plays a significant role in determining the oxidation locus, which is only affected subtly by the geometric distortions afforded by backbone length.

Thomas and coworkers recently reported the solid-state structure of $[Cu\mathbf{9}]^+$, providing the first example of an unambiguous Cu-salen metal-phenoxyl radical structure (Figure 5) [45]. The complex displays a non-symmetric coordination sphere change, in which the phenoxyl radical unit is characterized by an increased Cu - O bond length and a decreased O - C bond length (Δ 0.09 Å and Δ −0.06 Å, respectively) relative to the neutral Cu^{II} species. The other ring displays phenolate-like metrical characteristics, suggesting a localized ligand radical exists in the solid state. Interestingly, the SbF_6^- counter-anion is positioned in close proximity to the phenoxyl bearing ring, presumably stabilizing the build-up of positive charge and facilitating radical localization. A similar hole localization is observed for $[Ni\mathbf{9}]^+$ in the same report, but these effects may only result from crystal packing forces [45].

The solid state structure of $[Ni\mathbf{11}]^+$, which possesses inherent electronic asymmetry, also shows an asymmetric coordination change. The amino-phenolate Ni-O bond is lengthened by 0.04 Å relative to Ni**11**, suggesting that the hole is localized predominately on the half of the ligand that was initially more electron rich [35]. In the case of [Cu**3**]$^+$, a weak axial interaction between the metal ion and a fluorine atom of the SbF_6^- counter-anion exists (2.76 Å), presumably stabilizing the high-valent Cu^{III} center (Figure 6) [46].

Interestingly, a third motif in which the oxidation locus resides on the dimethoxy substituted diiminobenzene bridge of a Cu(II) salen complex has recently been observed by Kochem *et al.* [47]. In the solid state structure of the one-electron oxidized complex, the C - O bond lengths of the phenolate rings are not contracted significantly, contrary to that anticipated for a phenoxyl radical type complex. In contrast, the two O - C bonds of the methoxy groups to the diiminobenzene backbone are contracted (Δ -0.01 and -0.018 Å), suggesting significant radical localization on the extended **π**-system of the phenylene backbone [47].

5.2. X-ray absorption spectroscopy

Metal K-edge X-ray absorption spectroscopy (XAS) is a powerful tool for determining metal coordination metrical parameters and the locus of oxidation in metal complexes. Solution EXAFS analysis allows for metrical assessment of complexes unstable in the solid-state, and provides a means for verifying structural similarity between species in solution versus solid-state in which crystal packing effects may lead to geometric differences. For metal-salen complexes, the average metrical parameters in solution generally do not differ significantly from those in the solid state.

Unlike other spectroscopic techniques, XAS is element specific and directly probes atomic effective nuclear charge from which metal oxidation state can be empirically correlated. The metal K-edge 1s → 3d transition, or pre-edge, has been used successfully to determine the oxidation state of metal ions in various metal-salen complexes [32,35,46,48]. Copper K-edge has been used to infer indirectly the formation of a phenoxyl radical upon oxidation of Cu**1**^{tBut2} [32]; the copper pre-edge feature for solid state samples of Cu**1**^{tBu2} and [Cu**1**^{tBu2}]$^+$ both lie at 8979 eV, consistent with the copper centers retaining a 2^+ oxidation state and ligand based oxidation. In the case of Cu**3**, however, the pre-edge feature shifts from 8979.2 to 8980.2, consistent with metal based oxidation and the formation of a Cu^{III} species upon oxidation (Figure 7) [46].

More recently, sulfur K-edge spectroscopy has been used to probe the hole character on alkyl sulfanyl phenolate substituents of oxidized Cu-salen complexes, providing potential insight into the influence of the Cys272 crosslink of GO [19,20]. Sulfur K-edge spectra of neutral Cu**12**^{SMe2} and Cu**12**^{SiPr2} are dominated by intense main-edge features at *ca.* 2474 eV. These features shift to higher energy for the oxidized complexes with a larger shift observed for [Cu**12**^{SMe2}]$^+$ than [Cu**12**^{SiPr}]$^+$. Such shifts are consistent with an increase of sulfur effective nuclear charge upon oxidation. The oxidized forms also exhibit an additional pre-edge feature at *ca.* 2471 eV, which is attributed to a S_{1s}-to-phenoxyl singly unoccupied molecular orbital (SUMO) transition, the intensity of which reflects the degree of sulfur *p*-orbital mixing into the SUMO [49]. Analysis of this feature yields sulfur contributions to the phenoxyl hole of 13% and 8% for [Cu**12**^{SMe2}]$^+$ and [Cu**12**^{SiPr2}]$^+$, respectively (Figure 8) [19]. DFT calculations suggest that an orientation of the less sterically demanding -SMe substituent in plane with the phenoxyl ring maximizes S *p*-orbital overlap with the aromatic **π** system in [Cu**12**^{SMe2}]$^+$, allowing for greater delocalization of the hole onto the sulfur atoms [19]. In a recent sulfur K-edge XAS study of GO_{ox} itself, Rokhsana *et al.* report a sulfur contribution from the Cys-Tyr cross link to the tyrosyl hole of 24 ± 3 % [50]. This value is in good agreement with previous electron paramagnetic resonance (EPR) studies of apo-GO_{ox} that predicted a value of 20 ± 3 % [51].

5.3. UV-Visible spectroscopy

UV-Visible (UV-Vis) spectra of neutral salen complexes typically contain a broad band of intense features near 25000 cm^{-1} (400 nm), arising from a combination of ligand-to-metal charge transfer (LMCT) and/or Schiff base π - π^* transitions. Several *d-d* transitions are also observed near 20000 - 16000 cm^{-1} (500 - 600 nm). In complexes with reduced imine bonds, Schiff-base transitions are eliminated and features near 25000 cm^{-1} tend to exhibit much lower intensity (ε < 2000 M^{-1} cm^{-1} vs 10000 M^{-1} cm^{-1}). In contrast to the neutral complexes, the spectral features of one- and two-electron oxidized complexes are dependent heavily on the substituents of the phenolates.

UV-Vis spectra of oxidized metal-salen complexes bearing -OMe and/or -SR substituents are dominated by intense absorptions near 22000 and/or 16000 cm^{-1} (*ca.* 450 and/or 600 nm), assigned to intra-ring methoxy-aryl π - π^* or sulfur-aryl π - π^* transitions, respectively. In non-symmetric complexes, sequential oxidation of the two phenolates is evident clearly by monitoring these substituent dependent absorptions [20,38]. For example, the spectrum of [Cu**14**$^{\mathrm{SiPr,OMe}}$]$^+$ shows an intense feature near 22000 cm^{-1}, assigned as a methoxy-aryl π - π^* transition, and relatively little intensity in the region expected for a sulfur-aryl π - π^* transition (Figure 9a). The -OMe bearing phenolate is oxidized more readily since this substituent is more electron donating. A subsequent oxidation to afford [Cu**14**$^{\mathrm{SiPrOMe}}$]$^{2+}$ leads to the appearance of an additional feature near 16000 cm^{-1}, consistent with oxidation of the -S^{i}Pr substituted phenolate (Figure 9b).

Spectrophotometric titration of Cu**14**$^{\mathrm{tBu,SiPr}}$ with one equivalent of chemical oxidant leads to growth of a sulfur-aryl absorption near 16000 cm^{-1}, the intensity of which does not change significantly following addition of a second oxidizing equivalent [20]. The removal of the second electron is assigned to the oxidation of the -^{t}Bu bearing phenolate, a change that contributes little to the optical spectrum in the visible range. Oxidized Mn-salen complexes bearing -OMe substituents display similar methoxy-aryl π -π^* transitions near 22000 cm^{-1}, suggesting that phenoxyl radicals are indeed generated upon oxidation and that different metal ions can lead to similar optical features [38].

5.4. Near-infrared spectroscopy

While UV-Vis transitions are useful for characterizing phenoxyl radical complexes, near-infrared (NIR) bands, attributed to phenolate-to-phenoxyl IVCT transitions, are often more diagnostic. While the presence of NIR transitions alone may suggest the formation of phenoxyl-radical complexes, a quantitative analysis of band-shape parameters provides a wealth of information regarding the mixed-valent nature and the degree of radical delocalization. In Class I systems, the electronic coupling coefficient (H_{AB}) between the two redox centers is negligible, and no IVCT transition is observed [22]. Class II mixed-valent compounds typically display broad, weak IVCT transitions ($\Delta\nu_{1/2} \geq 2000$ cm^{-1}, $\varepsilon \leq 5000$ M^{-1} cm^{-1}), the energies of which are dependent on solvent dielectric [22]. Class III molecules have intense, narrow IVCT bands ($\Delta\nu_{1/2} \leq 2000$ cm^{-1}, $\varepsilon \geq 5000$ M^{-1} cm^{-1}), the energies of which are solvent independent, as no significant change in dipole moment results from electron transfer from the ground state to excited state. In the Class II regime, band-shape parameters and $\Delta\nu_{\mathrm{HTL}}$ (equation 1) are used to calculate H_{AB} (equation 2).

The majority of Cu-salen phenoxyl radical complexes display Class II like behavior, regardless of phenolate substitution pattern. We have recently reported the band-shape analysis of a series of non-symmetric Cu-salen phenoxyl radical complexes ([Cu**14**$^{\mathrm{R1,R2}}$]$^+$), the values of H_{AB} for which average at 2100 ± 200 cm^{-1} despite the different functional groups and wide range of IVCT ν_{max} values (Table 2). Similarly, all [Cu**13**$^{\mathrm{R1,R2}}$]$^+$ complexes have H_{AB} values centered at 1800 ± 200 cm^{-1}.

[Ni**3**]$^+$ by contrast displays a very intense (ε = 21500 M^{-1} cm^{-1}) and narrow transition at 4700 cm^{-1} (2100 nm), consistent with delocalization of the radical (consistent with DFT calculations) that suggests a Class III description with a Ni^{II} center and ligand radical (Figure 10) [40]. Upon addition of exogenous pyridine, this feature disappears, in line with EPR results that indicate the formation of a $Ni^{III}(py)_2$ species [37,40]. The palladium and platinum analogues of [Ni**3**]$^+$ also show intense IVCT transitions in the NIR, the intensity of which increases in the order Pt > Ni > Pd, with the former two best described as Class III and [Pd**3**]$^+$ best described as Class II (Figure 11) [43]. This coincides with the asymmetric quinoid-like crystal structure of [Pd**3**]$^+$$SbF_6^-$[43].

The "half-reduced" complex Ni**11**, which differs only in a single imine to amine bond compared to Ni**3**, shows markedly different behavior. One-electron oxidation of Ni**11** leads to formation of a Class II mixed valent species, as evidenced by the attenuation of the intensity of the NIR transition (*ca.* 2000 M^{-1} cm^{-1}, Figure 12) [35]. Presumably, the radical is localized on the formerly more electron rich amino-phenolate, suggesting that ostensibly subtle ligand perturbations can lead to significant changes in the electronic properties of these complexes.

Kurahashi and Fujii have investigated recently a series of non-symmetric manganese and nickel salen complexes. One-electron oxidation of these compounds results in the formation of phenoxyl radical complexes, with the hole localized on the phenolate that was originally more electron rich, as evidenced by the UV-Vis optical features. Interestingly, the energies of the IVCT transitions correlate directly to the electron donating/withdrawing properties of the phenolate substituents. For example, [Mn**14**^{OMe2}]$^+$ exhibits a broad IVCT transition at 7870 cm^{-1} (1270 nm), while [Mn**14**^{tBu,OMe}]$^+$ and [Mn**14**^{ClOMe}]$^+$ display IVCT transitions at 9850 cm^{-1} (1015 nm) and 11200 cm^{-1} (890 nm), respectively [38]. In all cases, the phenoxyl radical localizes on the -OMe bearing phenolate. A shift to higher energy observed for the IVCT bands of [Mn**14**^{tBu,OMe}]$^+$ and [Mn**14**^{ClOMe}]$^+$ relative to [Mn**14**^{OMe2}]$^+$ correlates to the electron withdrawing ability of the substituent on the unoxidized donor phenolate (−Cl > −^{t}Bu > −OMe) [38]. However, the IVCT transition energies of [Cu**13**^{R1,R2}]$^+$ and [Cu**14**^{R1,R2}]$^+$, bearing combinations of −^{t}Bu, −S^{i}Pr, and −OMe substituents, do not show a simple relationship to the electronic properties of the un-oxidized donor phenolate. This may suggest that the trend described by Kurahashi and Fujii is not general. In all observed cases, subsequent oxidation to form two-electron oxidized salen complexes results in the disappearance of NIR transitions, consistent with the formation of a bis-phenoxyl radical species lacking IVCT bands [20,29].

Kurahashi and coworkers previously reported the study of one- and two- electron oxidized iron(III) salen complexes that display interesting optical features. One-electron oxidation to afford a Fe(III)-phenoxyl radical complex ($S = 2$) results in broad absorptions near 12800 and 11000 cm^{-1} (780 and 870 nm) [52]. A second oxidation to yield the two-electron oxidized complex ($S = 3/2$) results in a doubling of intensity and red-shift of this feature to 10900 cm^{-1} (913 nm) [52]. No additional absorptions from 9000 – 4000 cm^{-1} (1100 – 2500 nm), the range expected for IVCT transitions in other metal-salen phenoxyl radical complexes, were observed for either the one- or two-electron oxidized complexes. Allard and coworkers reported the study of an N_2O_3 five-coordinate Fe(III) phenoxyl radical complex bearing a salen like ligand with a pendant phenolate arm axially coordinated to the iron center. One electron oxidation leads to localization of the phenoxyl radical on a single phenolate moiety, the identity of which varies depending on the nature of the ligand electronics [41]. Interestingly, both complexes studied show an absorption feature near 13000 cm^{-1} (750 nm), which is assigned as a high-energy IVCT transition [41].

5.5. EPR spectroscopy

Neutral Cu^{II}-salen complexes (d^9 ground state) are paramagnetic compounds that can be characterized by EPR spectroscopy. Generally speaking, X-band EPR spectra of frozen solutions of Cu^{II}-salen complexes display axial or rhombic signals, characteristic of monomeric, nearly planar complexes, with a $d_{x2\text{-}y2}$ ground state.

One-electron oxidation of Cu^{II}-salen complexes leads to various spectral changes, depending on the phenolate substitution pattern of the complexes. Upon oxidation, EPR signals for complexes bearing –^{t}Bu substituents, such as Cu**3** and Cu**4**, are attenuated substantially, suggesting the formation of (1) a diamagnetic Cu^{III}-phenolate species (d^8), (2) an anti-ferromagnetically coupled Cu^{II}-phenoxyl species, analogous to GO$_{ox}$, or (3) a ferromagnetic species with a large zero-field splitting parameter. It has been confirmed that case (1) applies to [Cu**3**]$^+$ at low temperatures while case (3) applies to complex [Cu**4**]$^+$ using other spectroscopic and theoretical methods [20,29,46]. Orio and coworkers have calculated a zero-field splitting parameter of 0.72 cm^{-1} for complex [Cu**9**]$^+$, a result that is consistent with the X-band EPR silence observed experimentally because the operating microwave frequency is typically on the order of 0.3 cm^{-1} [45]. Because dramatically different spin configurations can all lead to EPR silence, conclusions drawn for oxidized Cu^{II}-salen complexes should be carefully analyzed by integrating additional information from other spectroscopic or physical measurements.

Bulk magnetic susceptibility techniques can aid in clarifying ambiguous EPR measurements. Variable-temperature SQUID magnetometry can be applied to oxidized metal-salen complexes that are isolable as stable solids [46]. To date, these samples are generally limited to complexes containing imino-phenolate moieties, which tend to be more stable than their amino-phenolate partners upon oxidation. Variable temperature solution magnetic susceptibility measurements by Evan's method can be applied to a wider range of oxidized metal-salen complexes [46].

Oxidized complexes bearing alkyl-sulfanyl substituents show markedly different X-band EPR behavior. One-electron oxidation does not result in a loss of EPR intensity, rather, the signals broaden and the integration relative to their parent neutral forms remains relatively constant [19,20]. It is postulated that the larger inter-spin distance afforded by significant delocalization of the hole onto the sulfur atom(s) in the *para* position of the phenolates, leads to weaker electron-electron coupling to the copper center and a more diradical character [53].

EPR characterization of oxidized Ni-Salen complexes is often times straightforward because of the limited spin configurations. The EPR spectrum of [Ni**3**]$^+$ shows a broad signal attributed to an $S = \frac{1}{2}$ species at $g_{iso} = 2.045$, suggesting a predominantly ligand based unpaired electron (Figure 13) [40]. Shimazaki *et al.* investigated the temperature dependence of the locus of oxidation in [Ni**3**]$^+$, using variable temperature EPR [39]. Cooling the sample shifts the oxidation locus from the ligand to the nickel center, which presumably results from counter-anion (NO$_3^-$) binding at lower temperatures rather than a purely temperature dependent radical shift [37,39,40]. Interestingly, addition of 3 equivalents of exogenous pyridine (Py) to [Ni**3**]$^+$SbF$_6^-$ results in a rhombic EPR pattern, characteristic of a low-spin NiI^{II} complex with a d_{z2} electronic ground state [40]. In contrast to this result, Pierre and coworkers have reported that complex [Ni**7**]$^+$ exists as a phenoxyl radical anti-ferromagnetically coupled to a high-spin Ni^{II} center in an octahedral-like environment, a configuration that results in an isotropic EPR signal at $g = 2.22$ [37].

In a recent report by Kochem and coworkers, the effect of ligand protonation on the locus of oxidation in complex Ni**10** was investigated. The frozen solution EPR spectrum of [Ni**10**]$^+$

in CH_2Cl_2 exhibits a nearly isotropic signal centered at $g_{iso} \approx 2.01$, the hyperfine splitting of which is consistent with a ligand radical localized on the *N,N*-dimethylamino phenolate with significant radical character on the nitrogen atom (Figure 14) [54]. In contrast to this result, the frozen solution EPR spectrum of $[\mathrm{Ni}\mathbf{10}\mathrm{H}]^{2+}$ in CH_2Cl_2 displays a highly anisotropic $S = ½$ signal at $g_1 = 1.994$, $g_2 = 2.017$,and $g_3 \approx 2.045$ ($g_{iso} \approx 2.02$) [54]. These *g*-values are in good agreement with those calculated by DFT for a radical localized on the di-*tert*-butyl substituted phenolate, suggesting that protonation of the *N,N*-dimethylamino results in a chemically induced oxidation locus shift [54].

5.6. Electrochemistry

Results from cyclic voltammetry (CV) and/or differential pulse voltammetry (DPV) provide keen insights into the nature of metal-salen complex oxidation. In most cases, results indicate that complexes display two phenolate-based oxidation processes at potentials near or greater to the $Fc^{0/+}$ redox couple, with reduced salen complexes exhibiting oxidation potentials *ca.* 350 mV lower than complexes containing imino-phenolates. When considering symmetric salen complexes, the difference in potential between sequential oxidations is often correlated to the extent of radical delocalization in the one-electron oxidized complexes. The mixed valent mono-cations, $[\mathrm{M}\mathbf{X}]^+$, exist in equilibrium with their neutral and dicationic forms in solution, with the comproportionation constant K_c equal to $\log K_c = (\Delta E / 59\ \mathrm{mV})$ at 298 K. ΔE values larger than the statistical value of 36 mV, corresponding to a $K_c = 4$, imply thermodynamic stabilization of the one electron oxidized species through delocalization of the radical, or in other words, electronic coupling.

In non-symmetric complexes, a thermodynamic preference for oxidation of one phenolate over the other exists, and the electrochemical splitting between the first and second redox process is a combination of this thermodynamic difference and the magnitude of electronic coupling in the one-electron oxidized species [20]. In non-symmetric manganese and nickel complexes reported by Kurahashi and Fujii, the observed electrochemical features are often correlated to the substitution patterns of the redox active phenolates (Table 3). For complexes bearing -OMe substituents, the first anodic peak potentials remain relatively constant, increasing slightly as more electron withdrawing substituents are introduced on the other phenolate. This is consistent with preferential oxidation of the -OMe bearing phenolate. A similar trend is also observed for non-symmetric copper salen complexes [20].

5.7. Resonance Raman spectroscopy

Resonance Raman spectroscopy (rR) is another precise tool for studying phenoxyl radical species. The rR spectra of GO_{ox} obtained with 875 nm excitation by McGlashen *et al.* exhibits bands attributed to both unoxidized Tyr495 and tyrosyl radical Tyr272 (Figure 15) [55]. The band observed at 1487 cm^{-1} is *ca.* 30 cm^{-1} lower in energy than expected for a tyrosinate C - O ν_{7a} stretch, consistent with coordination of a tyrosyl O atom to the Cu^{II} metal center. Bands at 1479, 1595, and 1185 cm^{-1} are slightly higher than those anticipated for ring modes ν_{8b}, ν_{8a}, and ν_{9a}, consistent with a quinoid-like structure of a tyrosyl radical ring. Since these phenoxyl radical vibrations are enhanced by excitation at 875 nm, it is postulated that this region in the absorption spectrum of the enzyme is attributed to a tyrosine-to-tyrosyl IVCT transition [55].

Phenoxyl radical salen complexes have also been successfully characterized using rR spectroscopy with excitation in the visible range. $[\mathrm{Cu}\mathbf{4}]^+$ exhibits vibrations at 1495 and 1597 cm^{-1} with excitation at 413 nm (Figure 16). Interestingly, the presence of both phenoxyl and phenolate bands for $[\mathrm{Cu}\mathbf{4}]^+$ may indicate localization of the phenoxyl radical on a single phenolate on the timescale of the Raman experiment [46]. In contrast, $[\mathrm{Cu}\mathbf{3}]^+$ displays bands at 1530 and 1598 cm^{-1} that do not correlate with the expected pattern for a phenoxyl radical species, consistent with the formation of a Cu^{III}-bis-phenolate complex upon oxidation at the low temperatures of the experiment. Similar to [Cu**4**]$^+$, [Ni**11**]$^+$ displays rR features that can be assigned as phenolate and phenoxyl radical vibrations, consistent with NIR spectroscopic results that suggest [Ni**11**]$^+$ exists as a localized phenoxyl radical complex (Class II, Figure 17) [35]. Shimazaki and coworkers have reported rR for neutral and oxidized Ni**3**; the presence of bands at 1504 and 1605 cm^{-1} in the rR spectrum of [Ni**3**]$^+$ suggests this species exists as a phenoxyl radical and are assigned as ν_{7a} and ν_{8a} vibrational modes, respectively [48].

6. Conclusion

The greater realized role of tyrosyl and modified tyrosyl radicals in biological systems has lead to the development of numerous model systems to help elucidate their direct and indirect role in catalysis. Oxidized metal-salen complexes have proven to be useful models of GO_{ox} as similar spectroscopic features and patterns of reactivity are found. Developments in synthetic methodology have diversified the scope of salen ligands, enabling a fine tuning of the electronics of the phenoxyl radical complexes and construction of small-molecule analogues that reproduce the electronic asymmetry afforded by the Cys-Tyr cross link in GO. A variety of spectroscopic techniques can be used to probe the locus of oxidation and degree of radical delocalization in these mixed-valent one-electron oxidized compounds. In particular, study of IVCT transitions has contributed significantly to the understanding of the electronic distribution in these systems and provides a starting point for quantitative assessment of GO_{ox} as a mixed-valent species. The coupling of spectroscopic and electrochemical techniques with experimentally calibrated DFT methods provides even greater insights. Our understanding of the low energy absorption features of GO_{ox} is incomplete however, and further study of model systems and the enzyme itself is necessary to fully realize the role of the tyrosyl radical in enzymatic activity.

Acknowledgments

We dedicate this review to Professor E.I. Solomon in his 65th year.

References

1. Fontecave M, Nordlund P, Eklund H, Reichard P. Adv Enzymol Relat Areas Mol Biol. 1992; 65:147–183. [PubMed: 1570768]
2. Stubbe J. Adv Enzymol Relat Areas Mol Biol. 1990; 63:349–419. [PubMed: 2407066]
3. Stubbe J, van der Donk WA. Chem Rev. 1998; 98:705–762. [PubMed: 11848913]
4. Frey PA, Hegeman AD, Reed GH. Chem Rev. 2006; 106:3302–3316. [PubMed: 16895329]
5. Barry BA, Babcock GT. Proc Natl Acad Sci. 1987; 84:7099–7103. [PubMed: 3313386]
6. Debus RJ. Biochim Biophys Acta. 1992; 1102:269–352. [PubMed: 1390827]
7. Chen YR, Gunther MR, Mason RP. J Biol Chem. 1999; 274:3308–3314. [PubMed: 9920871]
8. MacMillan F, Kannt A, Behr J, Prisner T, Michel H. Biochemistry. 1999; 38:9179–9184. [PubMed: 10413492]
9. Whittaker MM, Kersten PJ, Nakamura N, SandersLoehr J, Schweizer ES, Whittaker JW. J Biol Chem. 1996; 271:681–687. [PubMed: 8557673]
10. Whittaker JW. Metal Ions in Biological Systems. 1994; 30(30):315–360.
11. Whittaker JW. Chem Rev. 2003; 103:2347–2363. [PubMed: 12797833]
12. Rogers MS, Dooley DM. Curr Opin Chem Biol. 2003; 7:189–196. [PubMed: 12714051]
13. Firbank SJ, Rogers MS, Wilmot CM, Dooley DM, Halcrow MA, Knowles PF, McPherson MJ, Phillips SEV. Proc Natl Acad Sci. 2001; 98:12932–12937. [PubMed: 11698678]
14. Ito N, Phillips SEV, Yadav KDS, Knowles PF. J Mol Biol. 1994; 238:794–814. [PubMed: 8182749]

15. Hockertz J, Steenken S, Wieghardt K, Hildebrandt P. J Am Chem Soc. 1993; 115:11222–11230.
16. Jazdzewski BA, Tolman WB. Coord Chem Rev. 2000; 200:633–685.
17. Thomas F. Eur J Inorg Chem. 2007:2379–2404.
18. Shimazaki Y, Yamauchi O. Indian Journal of Chemistry Section a-Inorganic Bio-Inorganic Physical Theoretical & Analytical Chemistry. 2011; 50:383–394.
19. Verma P, Pratt RC, Storr T, Wasinger EC, Stack TDP. Proc Natl Acad Sci. 2011; 108:18600–18605. [PubMed: 22065750]
20. Pratt RC, Lyons CT, Wasinger EC, Stack TDP. J Am Chem Soc. 2012; 134:7367–7377. [PubMed: 22471355]
21. Al-Noaimi M, Yap GPA, Crutchley RJ. Inorg Chem. 2004; 43:1770–1778. [PubMed: 14989670]
22. D'Alessandro DM, Keene FR. Chem Soc Rev. 2006; 35:424–440. [PubMed: 16636726]
23. Robin MB, Day P. Adv Inorg Chem Rad. 1967; 10:247.
24. Brunschwig BS, Creutz C, Sutin N. Chem Soc Rev. 2002; 31:168–184. [PubMed: 12122642]
25. Pfeiffer P, Breith E, Lubbe E, Tsumaki T. Justus Liebigs Annalen Der Chemie. 1933; 503:84–130.
26. Cozzi PG. Chem Soc Rev. 2004; 33:410–421. [PubMed: 15354222]
27. Baleizao C, Garcia H. Chem Rev. 2006; 106:3987–4043. [PubMed: 16967927]
28. Saint-Aman E, Ménage S, Pierre JL, Defrancq E, Gellon G. New J Chem. 1998; 22:393–394.
29. Pratt RC, Stack TDP. J Am Chem Soc. 2003; 125:8716–8717. [PubMed: 12862453]
30. Thomas F, Jarjayes O, Duboc C, Philouze C, Saint-Aman E, Pierre JL. Dalton Trans. 2004:2662–2669. [PubMed: 15514749]
31. Yao HH, Lo JM, Chen BH, Lu TH. Acta Crystallographica Section C-Crystal Structure Communications. 1997; 53:1012–1013.
32. Wang YD, DuBois JL, Hedman B, Hodgson KO, Stack TDP. Science. 1998; 279:537–540. [PubMed: 9438841]
33. Campbell EJ, Nguyen ST. Tetrahedron Lett. 2001; 42:1221–1225.
34. Wang Y, Stack TDP. J Am Chem Soc. 1996; 118:13097–13098.
35. Storr T, Verma P, Shimazaki Y, Wasinger EC, Stack TDP. Chem Eur J. 2010; 16:8980–8983. [PubMed: 20645357]
36. Connelly NG, Geiger WE. Chem Rev. 1996; 96:877–910. [PubMed: 11848774]
37. Rotthaus O, Thomas F, Jarjayes O, Philouze C, Saint-Aman E, Pierre JL. Chem Eur J. 2006; 12:6953–6962. [PubMed: 16810650]
38. Kurahashi T, Fujii H. J Am Chem Soc. 2011; 133:8307–8316. [PubMed: 21553916]
39. Shimazaki Y, Tani F, Fukui K, Naruta Y, Yamauchi O. J Am Chem Soc. 2003; 125:10512–10513. [PubMed: 12940721]
40. Storr T, Wasinger EC, Pratt RC, Stack TDP. Angew Chem Int Ed. 2007; 46:5198–5201.
41. Allard MM, Sonk JA, Heeg MJ, McGarvey BR, Schlegel HB, Verani CN. Angew Chem Int Ed. 2012; 51:3178–3182.
42. Sokolowski A, Bothe E, Bill E, Weyhermüller T, Wieghardt K. Chem Commun. 1996:1671–1672.
43. Shimazaki Y, Stack TDP, Storr T. Inorg Chem. 2009; 48:8383–8392. [PubMed: 19639970]
44. Shimazaki Y, Arai N, Dunn TJ, Yajima T, Tani F, Ramogida CF, Storr T. Dalton Trans. 2011; 40:2469–2479. [PubMed: 21290041]
45. Orio M, Jarjayes O, Kanso H, Philouze C, Neese F, Thomas F. Angew Chem Int Ed. 2010; 49:4989–4992.
46. Storr T, Verma P, Pratt RC, Wasinger EC, Shimazaki Y, Stack TDP. J Am Chem Soc. 2008; 130:15448–15459. [PubMed: 18939830]
47. Kochem A, Jarjayes O, Baptiste B, Philouze C, Vezin H, Tsukidate K, Tani F, Orio M, Shimazaki Y, Thomas F. Chem Eur J. 2012; 18:1068–1072. [PubMed: 22213540]
48. Shimazaki Y, Yajima T, Tani F, Karasawa S, Fukui K, Naruta Y, Yamauchi O. J Am Chem Soc. 2007; 129:2559–2568. [PubMed: 17290991]
49. Martin-Diaconescu V, Kennepohl P. J Am Chem Soc. 2007; 129:3034. [PubMed: 17319664]

50. Rokhsana D, Howells AE, Dooley DM, Szilagyi RK. Inorg Chem. 2012; 51:3513–3524. [PubMed: 22372371]

51. Lee YK, Whittaker MM, Whittaker JW. Biochemistry. 2008; 47:6637–6649. [PubMed: 18512952]

52. Kurahashi T, Kobayashi Y, Nagatomo S, Tosha T, Kitagawa T, Fujii H. Inorg Chem. 2005; 44:8156–8166. [PubMed: 16241166]

53. Rajca A. Chem Rev. 1994; 94:871–893.

54. Kochem A, Orio M, Jarjayes O, Neese F, Thomas F. Chem Commun. 2010; 46:6765–6767.

55. McGlashen ML, Eads DD, Spiro TG, Whittaker JW. J Phys Chem. 1995; 99:4918–4922.

Abbreviations

GO	galactose oxidase
GO$_{ox}$	oxidized galactose oxidase
IVCT	intervalence charge transfer
NIR	near-infrared
Th^{+}	thianthrenyl radical
XAS	X-ray absorption spectroscopy
SUMO	singly unoccupied molecular orbital
DFT	density functional theory
EPR	electron paramagnetic resonance
SQUID	superconducting quantum interference device
UV	ultraviolet
Vis	visible
LMCT	ligand-to-metal charge transfer
S	total spin state
g	*g*-value
CV	cyclic voltammetry
DPV	differential pulse voltammetry
K_c	comproportionation constant
rR	resonance Raman

Highlights

- We discuss metal-salen phenoxyl radical complexes in the context of galactose oxidase modeling
- Synthetic strategies for tuning electronic properties of salen ligands are discussed
- Emphasis is placed on spectroscopic and electrochemical characterization of phenoxyl radical complexes as mixed-valent species along with a Marcus-Hush analysis of their intervalence charge transfer bands

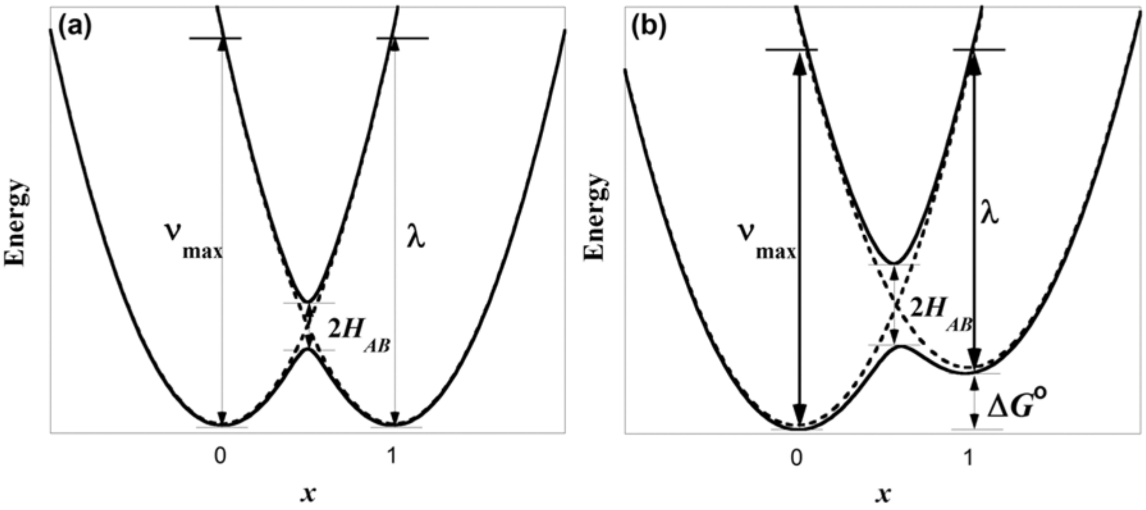

Figure 1.

Schemes of Marcus-Hush coupling in (a) symmetric and (b) non-symmetric mixed-valent complexes.

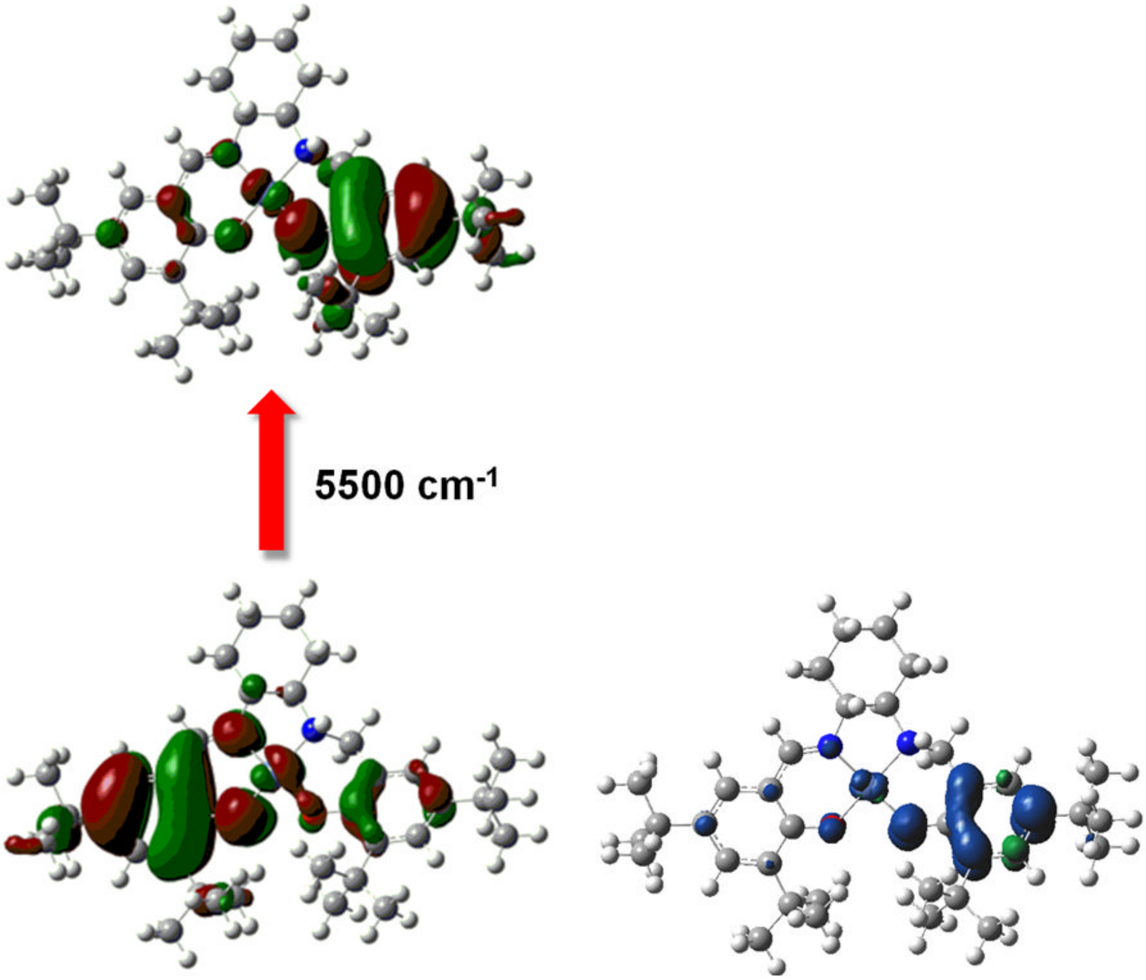

Figure 2.
(left) TD-DFT β-HOMO → β-LUMO transition for $[Ni11]^+$ and (right) spin density plot for $[Ni11]^+$ showing radical localization on the amino-phenolate [35].

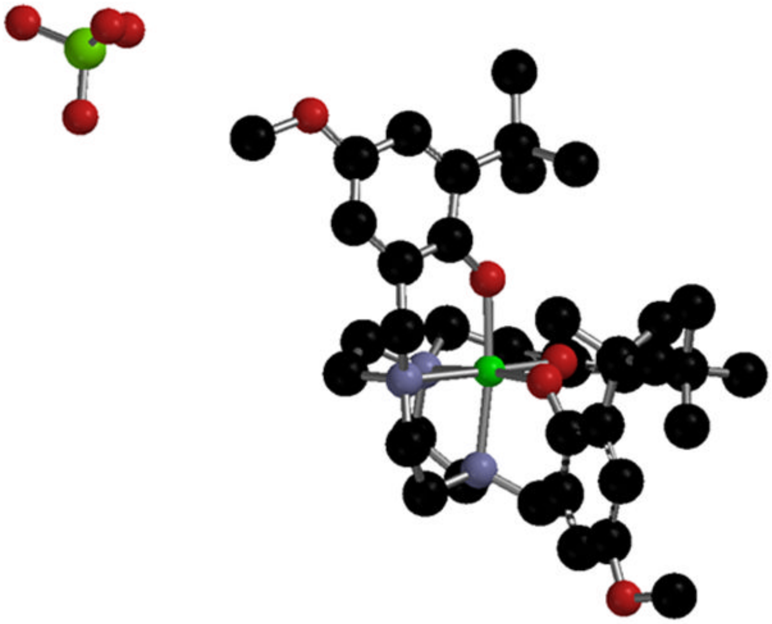

Figure 3.
X-ray structure of Cr-tacn phenoxyl radical complex [42].

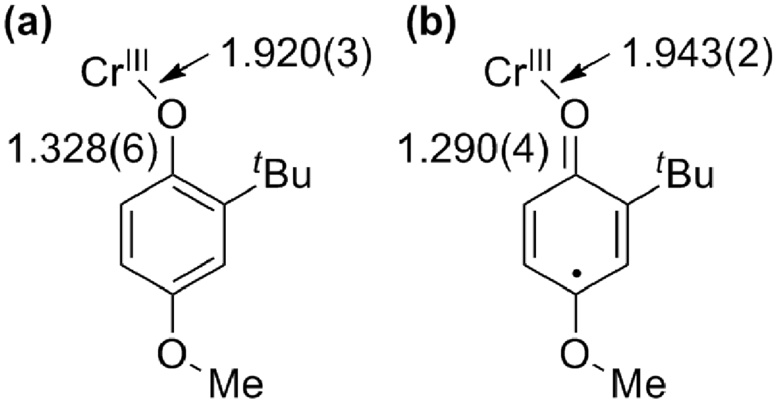

Figure 4.
Metrical parameters of (a) neutral and (b) oxidized Cr-tacn phenolate complex [42].

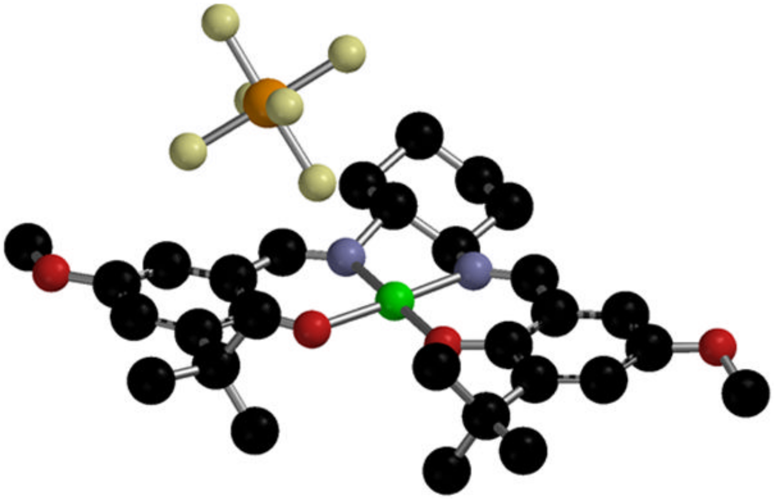

Figure 5.
X-ray structure of $[Cu9]^{+}SbF_6^{-}$ [45].

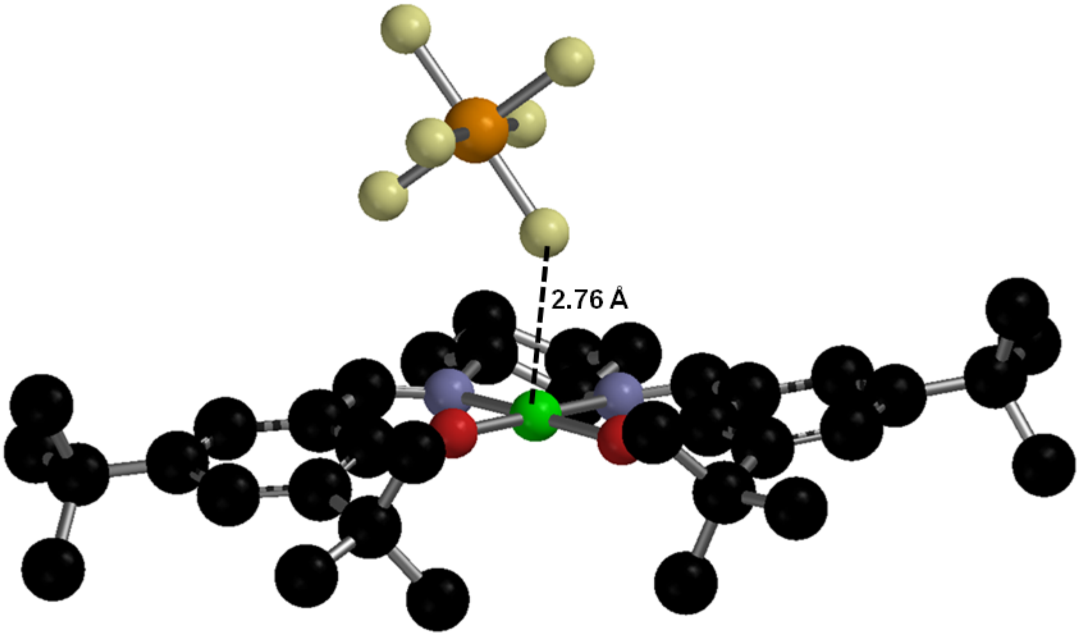

Figure 6.
X-ray structure of $[Cu3]^{+}SbF_6^{-}$ [46].

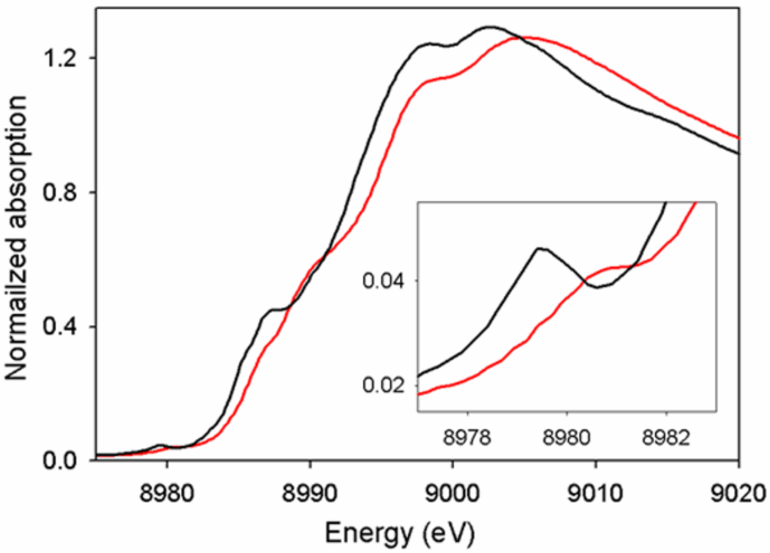

Figure 7.
Solid state Cu K-edge of Cu3 (black) and $[Cu3]^+SbF_6^-$ (red) inset: Cu pre-edge region (1s → 3d transition) [46].

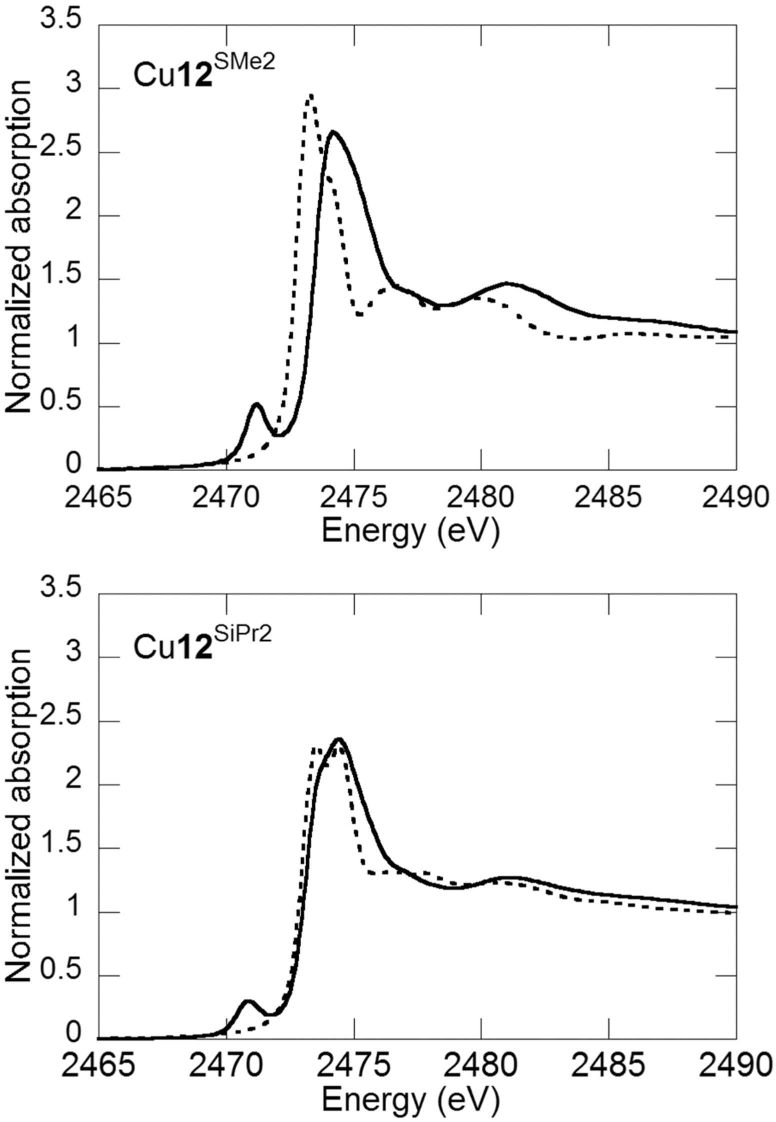

Figure 8.

Solid state sulfur K-edge of neutral (dotted) and oxidized (solid) complexes Cu12^{SMe2} and Cu12^{SiPr2}[19] .

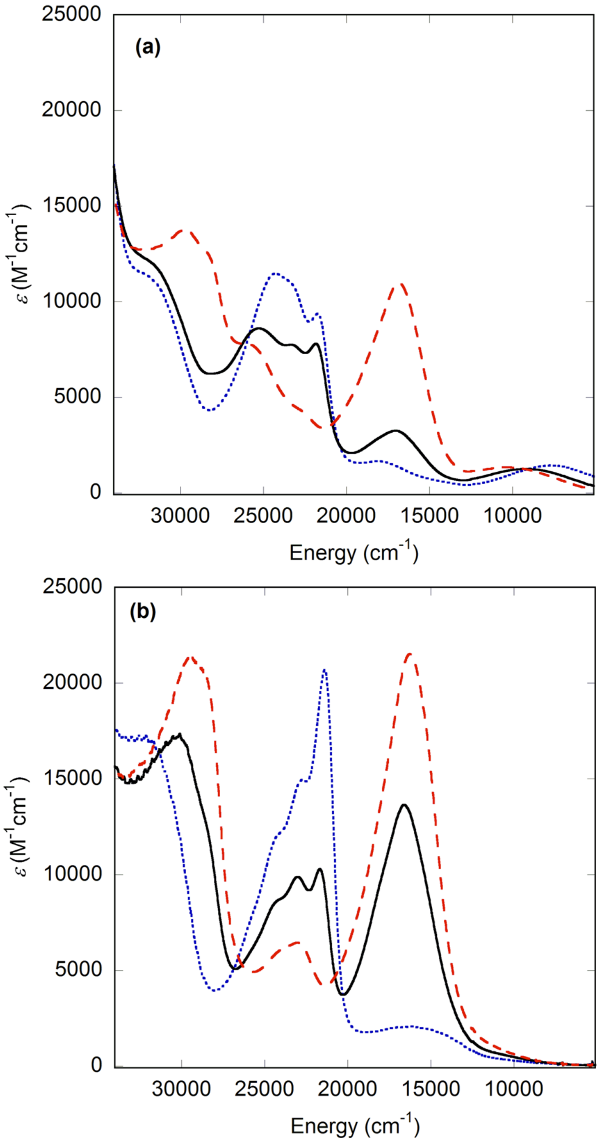

Figure 9.

(a) UV-Vis spectra of $[Cu9]^+$ (blue), $[Cu12^{SiPr2}]^+$ (red), and $[Cu14^{SiPr,OMe}]^+$ (black); (b) UV-Vis spectra of $[Cu9]^{2+}$ (blue), $[Cu12^{SiPr2}]^{2+}$ (red), and $[Cu14^{SiPrOMe}]^{2+}$ (black). Conditions; 0.1mM complex in CH_2Cl_2 at 298 K [20].

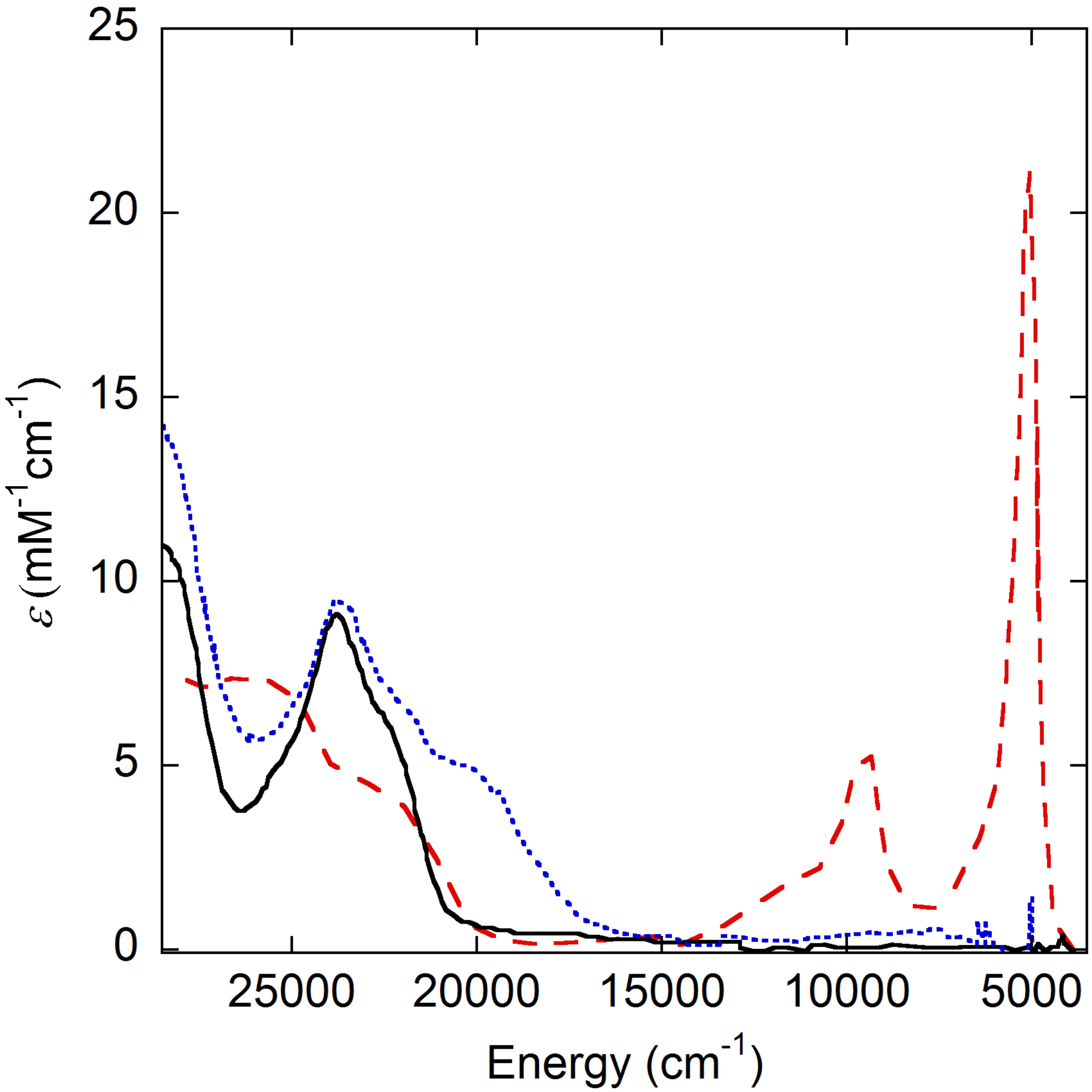

Figure 10.
UV-Vis-NIR spectra of Ni3 (black), [Ni3]$^+$ (red), and [Ni3]$^+$(py)$_2$ (blue). Conditions, 0.08 mM complex in CH_2Cl_2 at 298 K. [Ni3]$^+$(py)$_2$ in 1:1 CH_2Cl_2:pyridine [40].

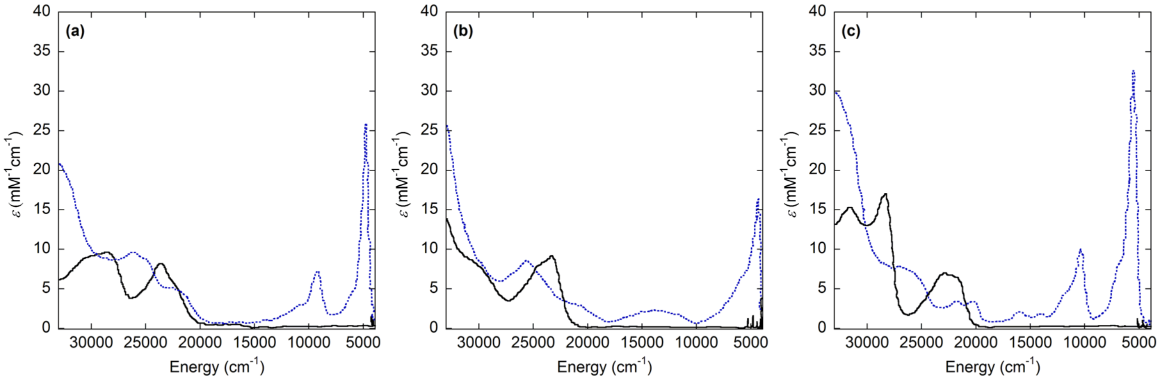

Figure 11.
UV-Vis-NIR spectra of neutral (black) and one-electron oxidized (red) group 10 metal-salen series: (a) Ni, (b) Pd, (c) Pt. Conditions; 0.1 mM complex, CH_2Cl_2 at 298K [43].

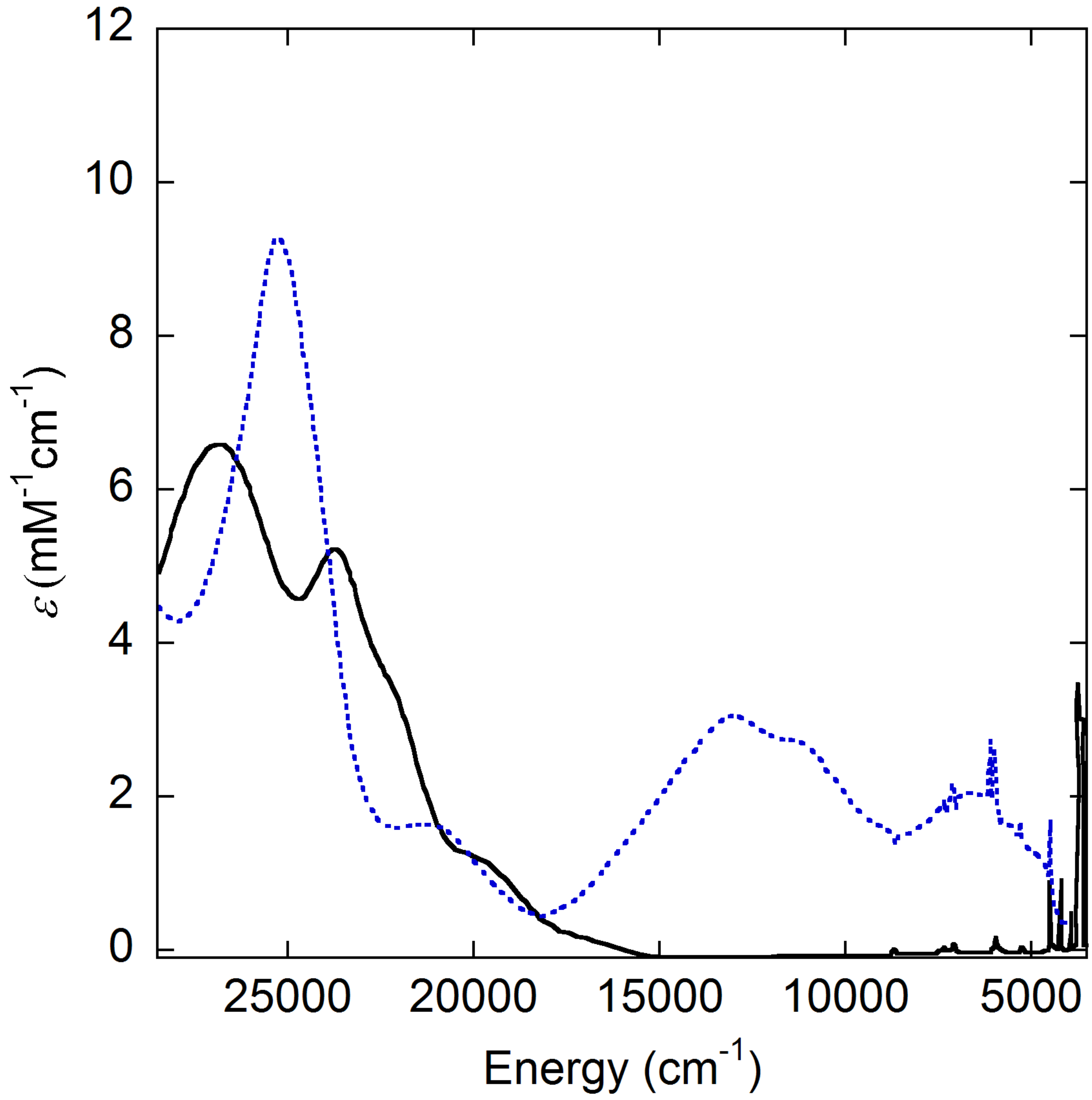

Figure 12.

UV-Vis-NIR of Ni11 (solid) and $[Ni11]^+$ (dashed). Conditions, 0.08 mM complex in CH_2Cl_2 at 298 K [35].

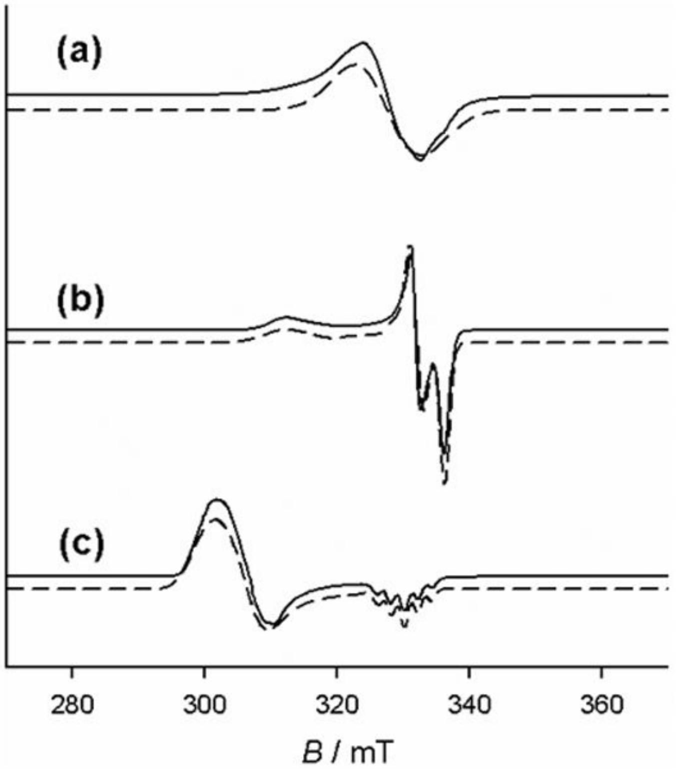

Figure 13.

X-band EPR spectra (solid: data; dashed: simulations) of (a) 1 mM $[Ni3]^+$, (b) 1 mM $[Ni3]^+$ + 0.1 M tetrabutylammonium perchlorate, (c) 1 mM $[Ni3]^+$ + 2 eq. pyridine. Conditions, 1 mM complex in frozen CH_2Cl_2 at 77 K [40].

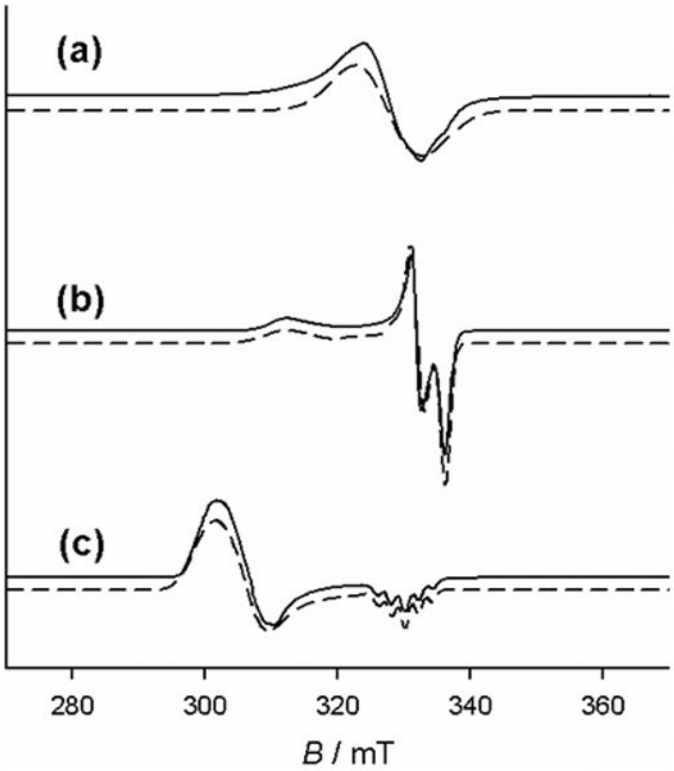

Figure 14.

X-band EPR spectra of (a) $[Cu10]^+$ and (b) $[Cu10H]^{2+}$. Conditions, 1 mM complex and 0.1 M tetrabutylammonium perchlorate in frozen CH_2Cl_2 at 77 K [54].

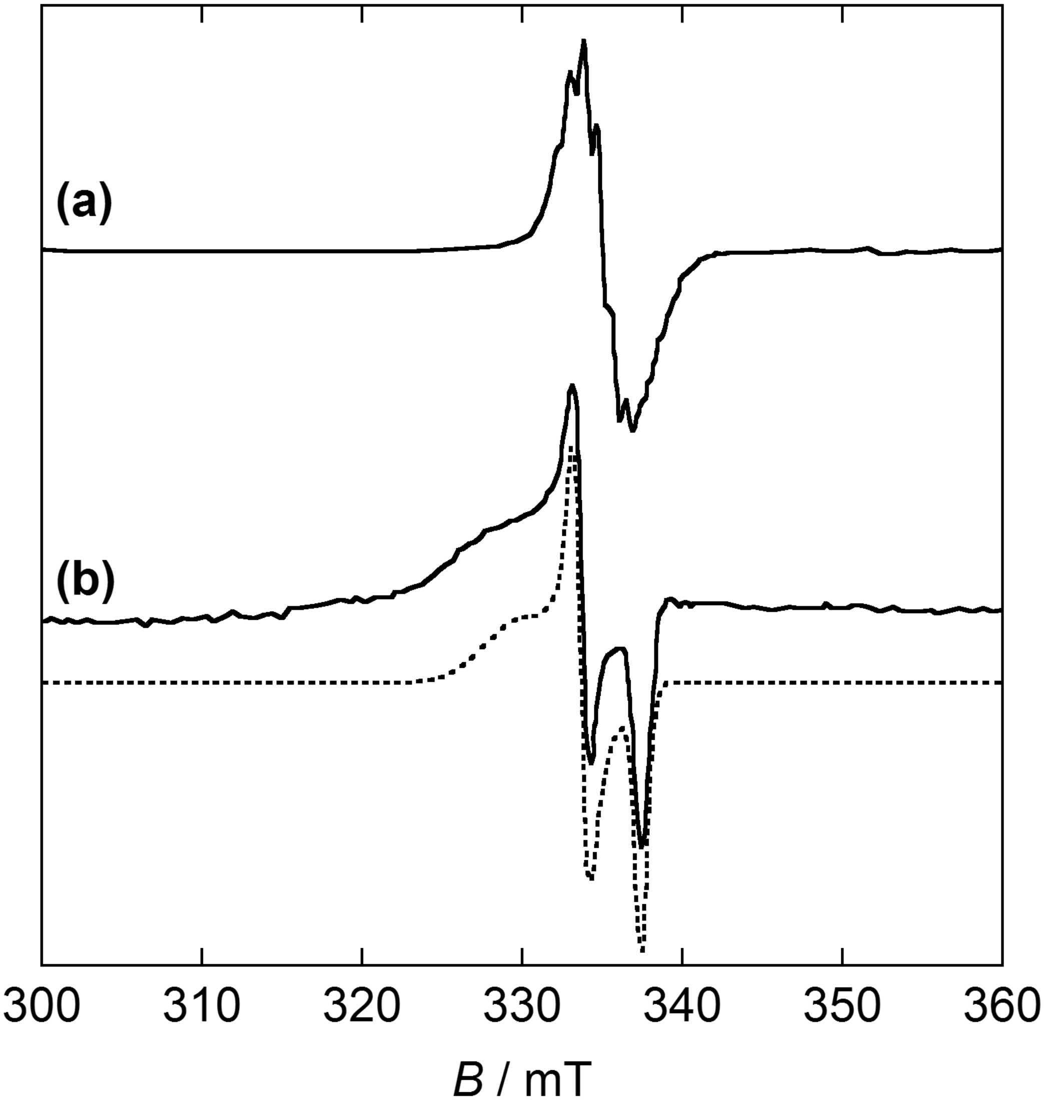

Figure 15.

Resonance Raman (rR) spectra of $\mathrm{GO_{ox}}$ (λ_{ex} = 875 nm) [55].

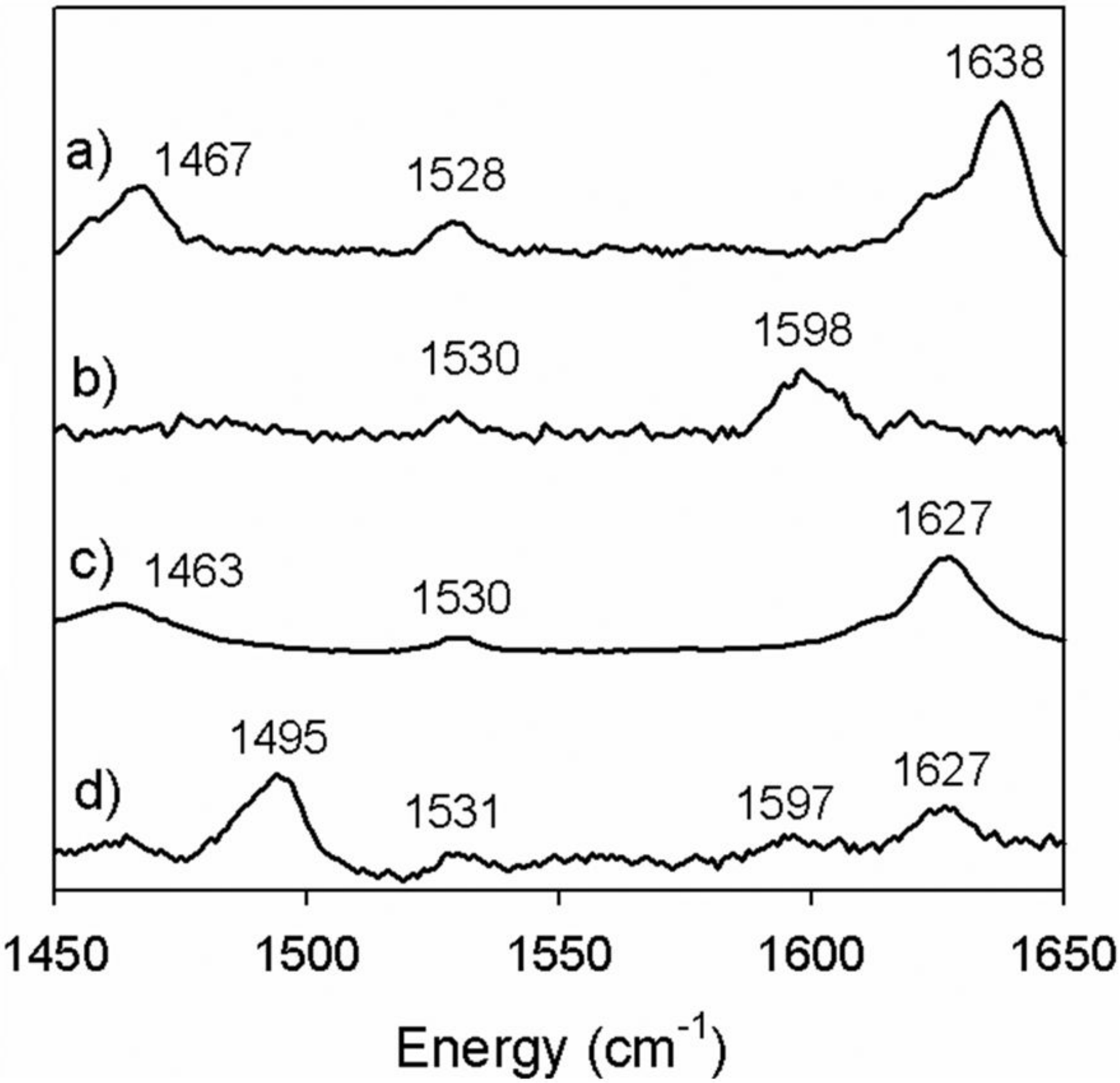

Figure 16.

Resonance Raman (rR) spectra of (a) Cu3, and (b) $[Cu3]^+$ at 298 K; rR spectra of (c) Cu4 and (d) $[Cu4]^+$ at 213 K (λ_{ex} = 413 nm). Conditions, 1 mM complex in CH_2Cl_2 [46].

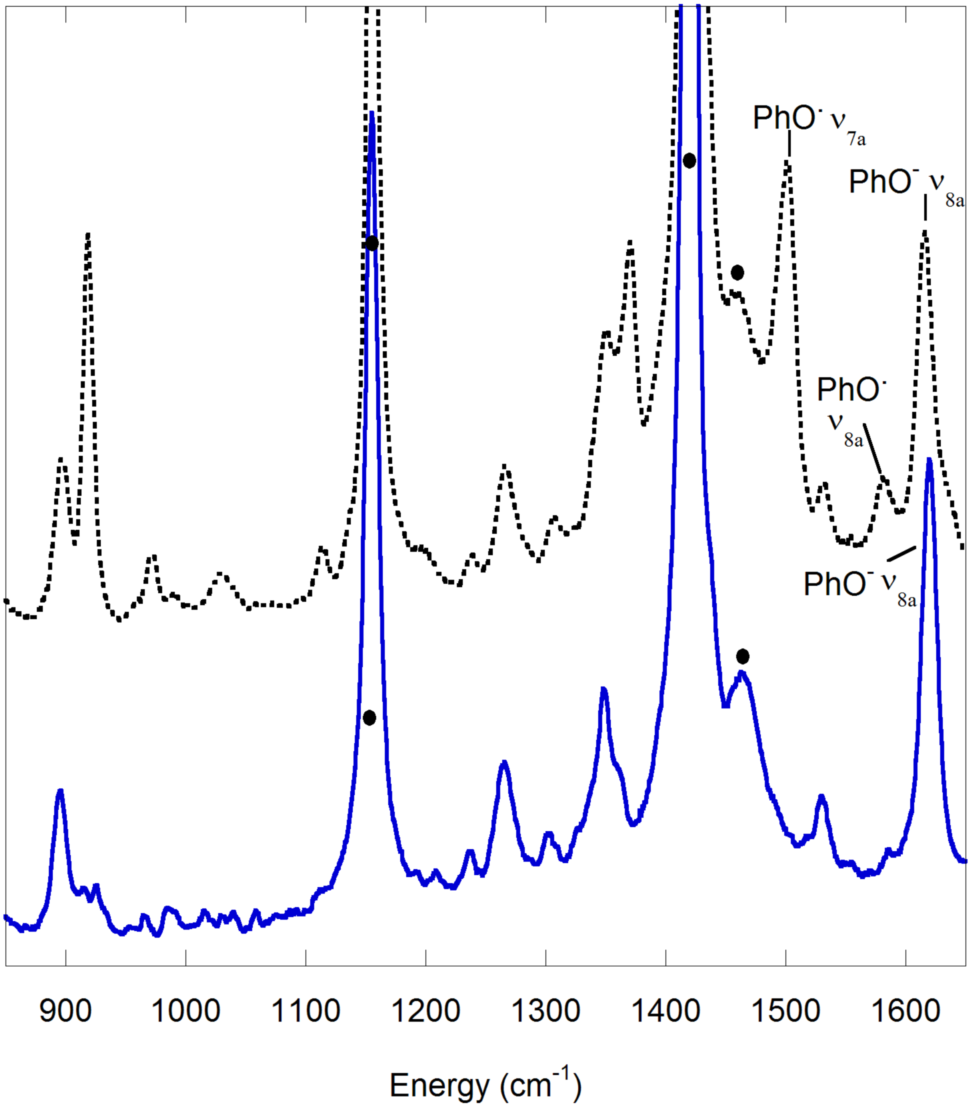

Figure 17.

Resonance Raman of Ni11 (solid) and $[Ni11]^+$ (dashed) in CH_2Cl_2 at 213 K (λ_{ex} = 413 nm). Solvent = • Conditions, 1 mM in CH_2Cl_2 at 213 K [35].

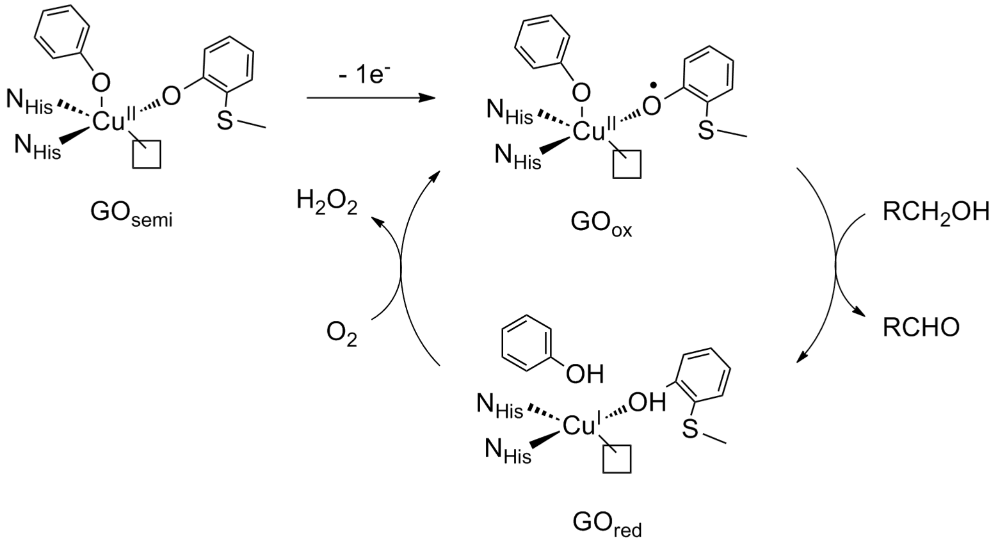

Scheme 1.

Consensus mechanism of GO.

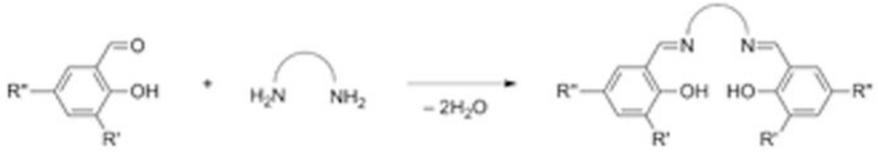

Scheme 2.
Generic salen condensation reaction.

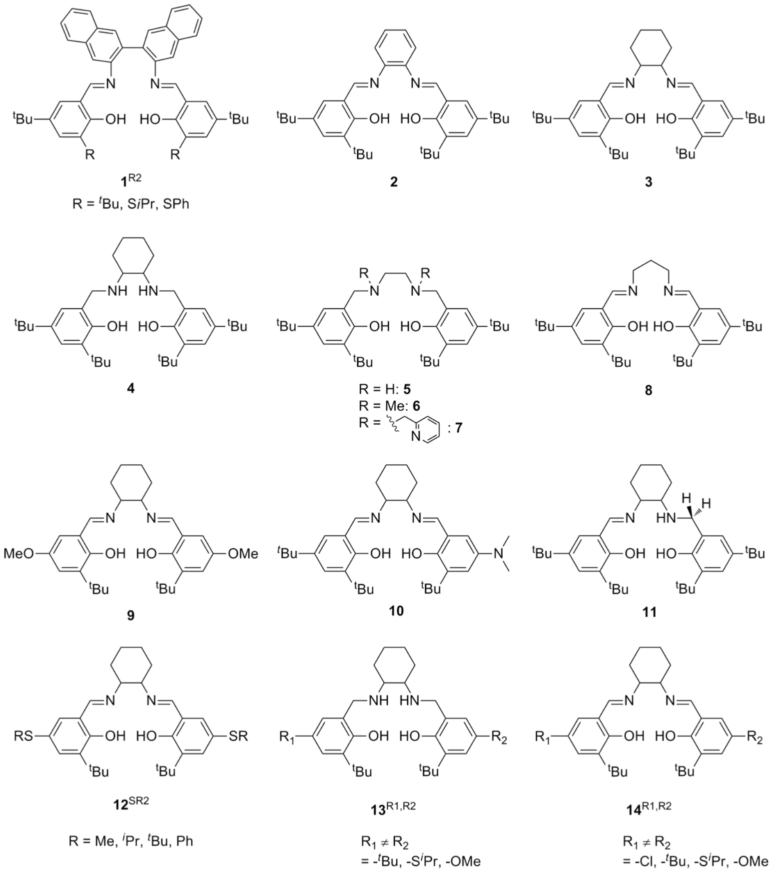

Scheme 3.
Salen ligands.

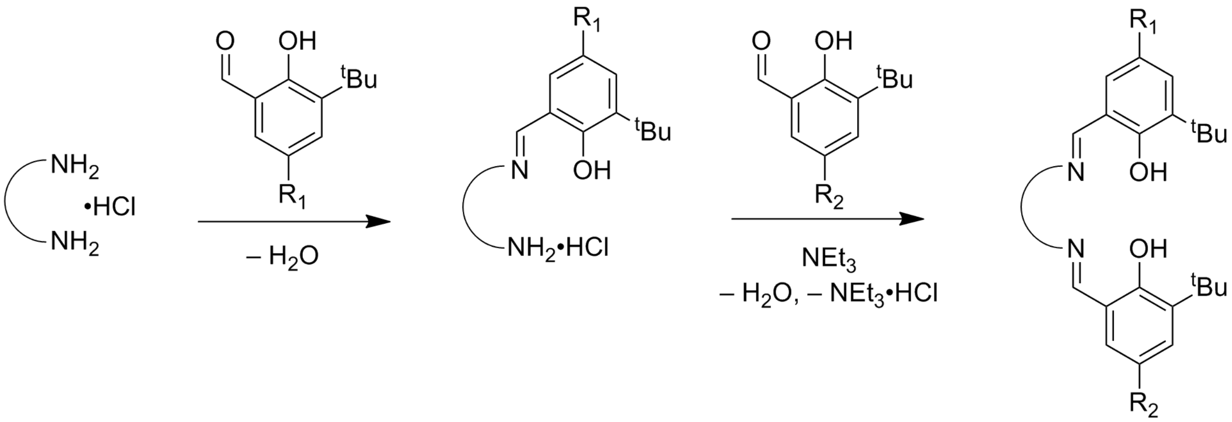

Scheme 4.

Synthesis of non-symmetric salen ligands.

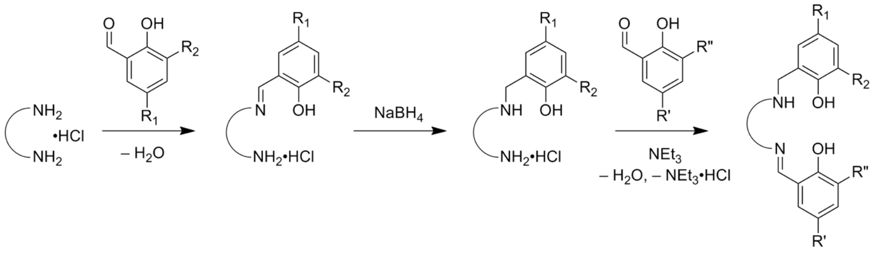

Scheme 5.

Synthesis of “half-reduced” salen ligands.

Table 1

Common chemical oxidants used to general metal-salen phenoxyl radicals [36].

Oxidant	**Solvent**	**$E°'$ (V) (vs Fc/Fc^+)**
$[NO]^+$	CH_2Cl_2	1.00
Ce(IV)	H_2O	0.88
Th^+	MeCN	0.86
$[N(C_6H_5Br\text{-}4)_3]^+$	CH_2Cl_2	0.70
Ag^+	CH_2Cl_2	0.65
$[Fe(\eta\text{-}C_5H_4COMe)_2]^+$	CH_2Cl_2	0.49
$[Fe(\eta\text{-}C_5H_4COMe)Cp]^+$	CH_2Cl_2	0.27

Table 2

IVCT analysis for $[\mathrm{Cu13}^{\mathrm{R1,R2}}]^+$ and $[\mathrm{Cu14}^{\mathrm{R1,R2}}]^+$ [20].

complex	ν_{max} (cm^{-1})	ε (M^{-1}cm^{-1})	$\Delta\nu_{1/2}$ (cm^{-1})	$\Delta\nu_{\mathrm{HTL}}$ (cm^{-1})	H_{AB} (cm^{-1})
$[\mathrm{Cu}\mathbf{14}^{\mathrm{tBu2}}]^+$	5700	2900	5600	3600	2300
$[\mathrm{Cu}\mathbf{14}^{\mathrm{tBu,OM2}}]^+$	8700	1400	5300	4500	1900
$[\mathrm{Cu}\mathbf{14}^{\mathrm{OMe2}}]^+$/ $[\mathrm{Cu}\mathbf{9}]^+$	7800	1400	6200	4200	2000
$[\mathrm{Cu}\mathbf{14}^{\mathrm{OMe,SiPr}}]^+$	9300	1200	6300	4600	2000
$[\mathrm{Ci}\mathbf{14}^{\mathrm{SiPr2}}]^+$/ $[\mathrm{Cu}\mathbf{12}^{\mathrm{SiPr}}]^+$	10200	1300	6200	4900	2200
$[\mathrm{Cu}\mathbf{14}^{\mathrm{tBu,SiPr}}]^+$	9300	1600	5800	4600	2200
$[\mathrm{Cu}\mathbf{13}^{\mathrm{tBu2}}]^+$	6300	2000	6200	3800	2100
$[\mathrm{Cu}\mathbf{13}^{\mathrm{tBu,OMe}}]^+$	9600	700	5400	4700	1500
$[\mathrm{Cu}\mathbf{13}^{\mathrm{OMe2}}]^+$	8300	1000	6200	4400	1700
$[\mathrm{Cu}\mathbf{13}^{\mathrm{OMe,SiPr}}]^+$	10500	900	5600	4900	1800
$[\mathrm{Cu}\mathbf{13}^{\mathrm{SiPr2}}]^+$	11200	900	6400	5100	2000
$[\mathrm{Cu}\mathbf{13}^{\mathrm{tBu,SiPr}}]^+$	10600	600	6900	4900	1600

Table 3

Substituent dependent redox potentials [38].

Complex	***E*° (V) (vs Fc/Fc$^+$)**
Mn**14**$^{\mathrm{OMe2}}$	0.51
Mn**14**$^{\mathrm{tBu,OMe}}$	0.52
Mn**14**$^{\mathrm{CI,OMe}}$	0.56
Ni**14**$^{\mathrm{OMe2}}$	0.26
Ni**14**$^{\mathrm{tBu,OMe}}$	0.28
Ni**14**$^{\mathrm{CI,OMe}}$	0.31